ACS Sustainable Chemistry & Engineering

pubs.acs.org/journal/ascecg

Research Article

Multisource Energy Harvester on Textile and Plants for Clean Energy Generation from Wind and Rainwater Droplets

Guanbo Min, Gaurav Khandelwal, Abhishek Singh Dahiya, Shashank Mishra, Wei Tang, and Ravinder Dahiya*

Cite This: ACS Sustainable Chem. Eng. 2024, 12, 695−705

Read Online

ACCESS | Metrics & More | Article Recommendations | Supporting Information

ABSTRACT: Distributed, clean, and sustainable energy solutions are needed to power sensor networks in applications such as the Internet of Things, digital agriculture, forests, smart homes, etc. Despite exploring various energy harvesters, their outputs achieved thus far are insufficient for driving low-power electronics in many of the abovementioned emerging applications. Herein, we present a textile-based multisource energy harvester, which can generate electricity from two clean energy sources, namely, triboelectric nanogenerator (TENG) and droplet-based electricity generator (DEG). The materials for the energy device are carefully selected, and their physical properties are tuned for higher energy output, primarily considering the following criteria: (i) maximum difference in the electron affinities, (ii) surface texturization, and (iii) hydrophobicity. The device mimics the water-repellent behavior of the lotus leaves ("lotus effect") to achieve a highly hydrophobic textile surface and enhance the output power. The optimized TENG part of the device generates 252 V and 57.6 μA during contact mode mechanical excitations and the DEG produces high output voltage and current of 113 V and 67 μA from waterdrops. Finally, the real-life application of the presented multisource energy harvesters is demonstrated by designing them as leaves of a synthetic plant, harvesting energy from wind and rain droplets to power light-emitting diodes.

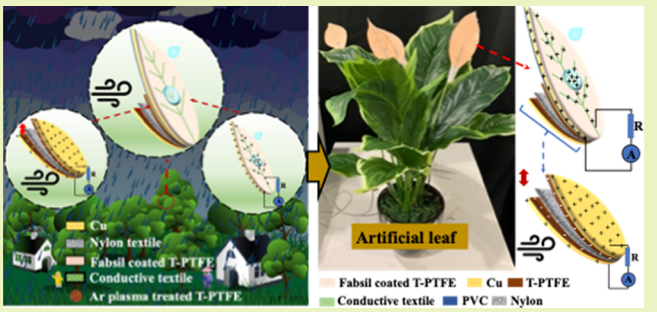

KEYWORDS: *clean energy, artificial leaves, triboelectric nanogenerators, droplet-based electricity generator, multienergy sources*

INTRODUCTION

Distributed sensor networks are needed for connected objects or the Internet of Things (IoT) in several conventional and emerging applications such as digital health, autonomous vehicles, smart homes and factories, environment monitoring, urban farming, etc.[1−6] The connected sensor network provides several advanced functions such as the capacity to sense vital human health parameters or crop/food quality[7−10] and react (actuation)[11,12] or respond (intelligence)[13−16] to external stimuli. For the reliable operation of any sensor network, it is important to have a stable power supply so that continuous data can be acquired from the sensors. Currently, most of the sensor networks are powered using either centralized conventional power plants or through energy storage devices such as lithium-ion batteries.[17] In the long term, such solutions are likely to have an adverse impact on the environment, as well as human health. For instance, lithium-ion batteries have drawbacks such as limited charge capacity, and thus their disposal will substantially contribute to environmental pollution due to the use of toxic materials.[18−22] On the other hand, longer use of conventional power stations, which depend on dwindling stock of fossil fuels, will only cause a delay in attaining the global net zero emission target. Noting these limitations, innovative green solutions are needed to power distributed sensor networks and mobile electronics and, in this regard, energy sources available in our natural environment such as wind, rain, light, ocean waves, etc. offer viable solutions.[23−27]

Most of the energy harvesters reported so far are designed to harness energy from a single source only, which may not be available all the time. For example, the output of solar cells considerably goes down during dark conditions.[27] Another example is wind-induced vibration-based devices, which have been shown to power several light-emitting diodes (LEDs) and a digital thermal sensor including displays.[28] However, just like solar cells, the energy is generated in the presence of wind. In this regard, a multisource energy harvester is attractive, as it could provide reliable power along with higher energy outputs. Among very few examples of multisource energy harvesters,

Received: June 14, 2023
Revised: December 10, 2023
Accepted: December 21, 2023
Published: January 2, 2024

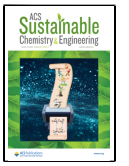

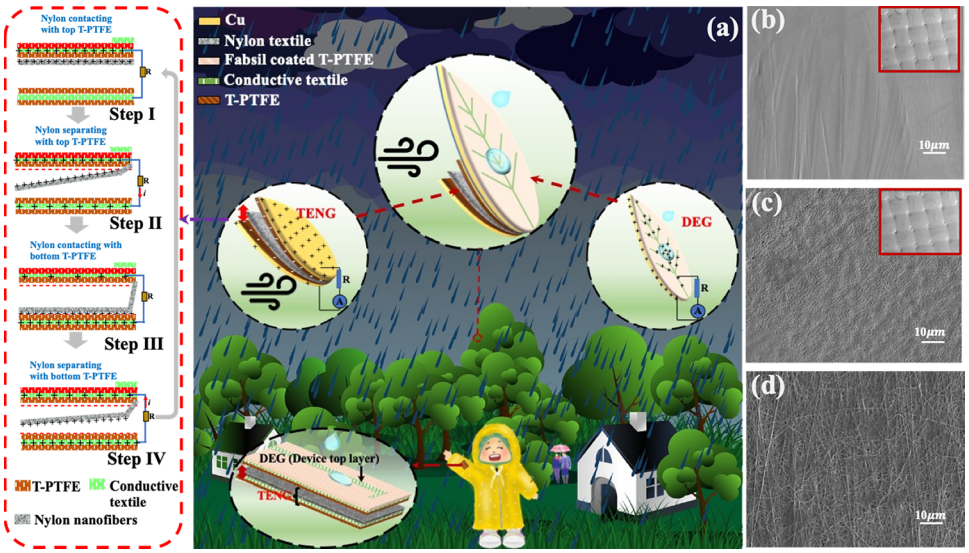

Figure 1. (a) Concept to harvest electricity from multisources, namely, wind and rain energy, by assembling TENG and DEG devices into artificial leaves. (b–d) Morphological analysis of the device materials: SEM images of (b) pristine T-PTFE, (c) Ar plasma-treated T-PTFE, and (d) nylon nanofibers.

the one based on rain energy is noteworthy, as it harnesses the electrostatic and kinetic energy impinged by a water droplet, which leads to high output power density (82.66 W/m^2) and transferred charge value (101 nC).[29]

Here, we present a leaf-shaped multisource energy harvester, which synergistically combines textile triboelectric nanogenerators (T-TENGs) and textile droplet-based electricity generators (T-DEGs). The synthetic decorative plants typically experience wind and rain in outdoor environments, and therefore, the presented multisource energy harvesting artificial leaves could be distributed and integrated to form artificial trees and plants to realize a mini green power station. This also aligns with newly emerging fields such as "plant nanobionics" or plant-hybrid technologies.[29] The T-TENGs are highly attractive for our devices because of excellent features such as flexibility, wider material choices with simple structural design, etc.[30] and can harvest electricity from biomechanical,[31,32] wind, and other ambient mechanical energy excitation.[33,34] Also, biomimetic textile is a unique class of material, as it offers advantages such as being soft, lightweight, and porous and is compatible with biodegradability and recyclability.[21,35] Biomimetic textiles with various forms of renewable energy harvesters based on mechanical,[36] thermal,[37] biochemical,[38] solar,[39] as well as hybrid energy forms[40] have been reported.

The materials used in this work are carefully selected, and their physical properties are further tuned for higher energy output, primarily considering the following criteria: (i) to have the maximum difference in the electron affinities, (ii) surface texturization, and (iii) hydrophobicity. Considering the first criterion, an interface material pair polytetrafluoroethylene (PTFE) textile (highly electronegative) and nylon-based nanofibrous materials (highly electropositive) are employed to fabricate high-performance T-TENG. Further, plasma treatments were performed to optimize their surface properties (surface texturization criterion) and thus enhance the surface tribo-charges. The optimized TENG device, fabricated using argon plasma-treated (100 W, 3 min) T-PTFE and nylon nanofibrous mats, shows about 50 times higher power density compared to the pristine T-PTFE device. The output power density compares well with the state-of-the-art values (Table S2). The DEG works through the coupling of triboelectric charging and the hydrophobic effect, which leads to remarkably high instantaneous output power.[34,41,42] Till date, a majority of the DEGs are reported using polymeric materials. In this work, inspired by the water-repellent behavior of the lotus leaves ("lotus effect"), we mimic the lotus effect to achieve a highly hydrophobic textile surface and, thus, enhance the output power. Toward this, molecular dynamics (MD) simulations were also performed so as to tune the water-repelling behavior of the textile surface (third criterion). The MD simulations allowed us to monitor the contact angles of the treated and untreated textile surfaces. An in-depth understanding of the DEG working mechanism and performance optimization parameters such as droplet falling height were also achieved by developing for the first time a DEG device model, which considers the dynamics of the droplet impact onto the DEG surface. The surface-modified textile-based DEG (T-DEG) exhibits the maximum output voltage and current of 113 V and 67 μA, respectively. As mentioned above, both the TENG and DEG were integrated to form a leaf-shaped device to harvest water droplet falling energy and wind energy. The leaf device design can operate under a dual mode: (i) conventional contact separation mode to harvest ambient wind energy and (ii) DEG to scavenge rain energy, as illustrated in Figure 1a. Four synthetic energy-generating leaves were implanted in a commercial artificial plant, and the output energy was measured under random rain drops and wind conditions. With the droplet impact, the maximum output voltage and short circuit current of DEG can reach 67.5 V and 10 μA, respectively. Simultaneously, the highest output voltage and short circuit current for wind energy harvesting can be 12 V and 1.75 μA, respectively. Finally, the potential applications of the fabricated energy leaves in applications such as IoT and smart lighting are demonstrated by powering 10 LEDs using the energy harvested from wind and rain.

EXPERIMENTAL SECTION

Materials. PTFE-based textile with a thickness of 200 μm and Fabsil (60% naphtha) was purchased from Amazon, U.K. The formic acid and Nylon-6,6 were purchased from Sigma-Aldrich.

https://doi.org/10.1021/acssuschemeng.3c03620
ACS Sustainable Chem. Eng. 2024, 12, 695−705

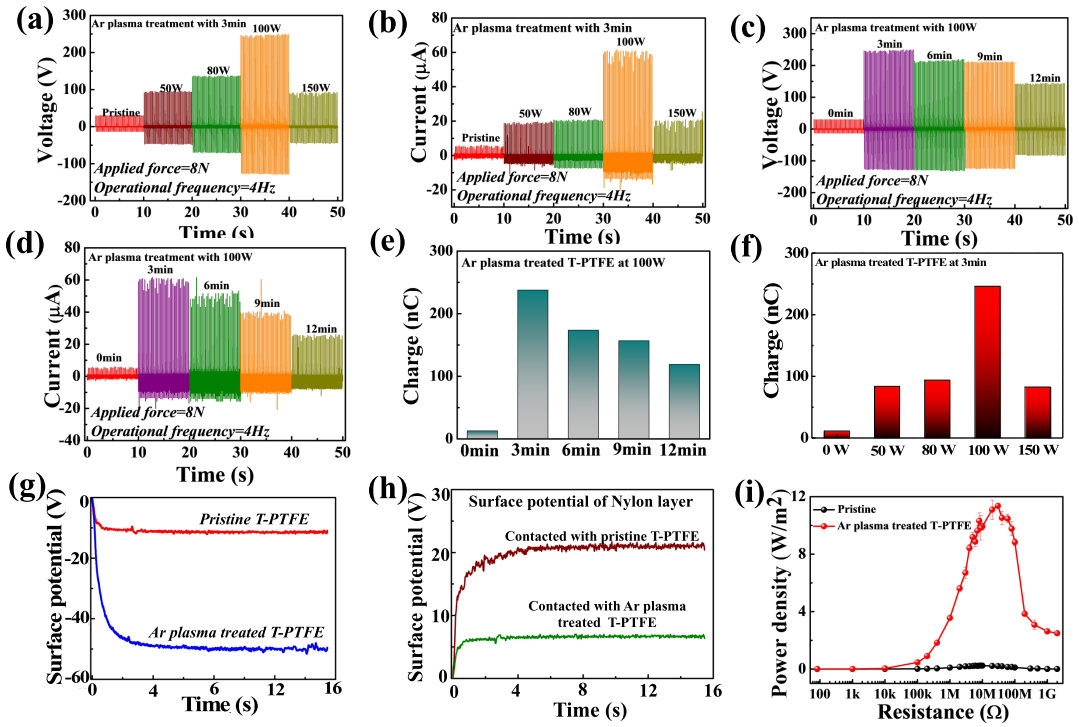

Figure 2. Performance of the T-TENG device. (a) output voltage and (b) short circuit current signals for the devices with T-PTFE under different Ar plasma powers. (c) Output voltage and (d) short circuit current signals for the devices with T-PTFE under different Ar plasma exposure time. The measured transferred charges for the devices with T-PTFE under (e) different Ar plasma exposure time and (f) different plasma generation power. Surface potential of (g) pristine and Ar plasma-treated T-PTFE. (h) Nylon surface which contacted with pristine and Ar plasma-treated T-PTFE. (i) Output power density across various resistive loads.

The plasma treatment was carried out in a flow of argon by an externally applied radio frequency field. First, four T-PTFE fabric samples were processed by Ar plasma for 3, 6, 9, and 12 min exposure time under a 100 W plasma power. After that, another four samples were treated under 50, 80, 100, and 150 W plasma power with a 3 min exposure time.

The nylon NFs were obtained using an electrospinning machine (TongLi, China). 9 wt % nylon powder was dissolved into the formic acid under 12 h stirring at 300 rpm and 25 °C. A 10 mL syringe was filled with the prepared nylon solution and connected to a spinneret with 17, 19, 20, and 22 G needles to obtain four variants of nylon NFs with different diameters. A 16 kV high voltage and a 2 mL/h flow rate were applied for electrospinning the nylon solution with a 15 cm distance between the needle and drum collector. The nylon NFs were collected by an aluminum foil-covered drum collector driving with a −2 kV voltage and a 1500 rpm rotating speed. The thickness of four nylon NFs mats was confirmed as 8 μm by a contact profiler.

The T-PTFE fabric was dipped in a commercial Fabsil solution for 20 min, followed by drying for further use.

T-TENG and T-DEG Fabrication. The nylon NFs were transferred onto a conductive fabric tape (Cu/Ni-based fabric tape with conductive adhesive) as the tribo-positive layer. The conductive fabric tape also bonds with the T-PTFE fabric to behave as a tribo-negative layer. Both tribo-positive and negative layers were cut as 4 × 2.5 cm^2 small pieces. To avoid a bulge, the electrodes and lead wires interfacing were mismatched at a fixed nominal contact area of 2.5 × 2.5 cm^2 during the measurements. The T-DEG device was fabricated by placing a T-PTFE layer on top of the T-TENG device. The copper and textile tape with different widths act as the top electrode of the T-DEG device.

Characterization. The surface roughness of the T-PTFE samples was measured by an optical profilometer (Bruker Contour GT-X 3D, Germany). The surface morphology of T-PTFE and nylon NF mats was characterized by FEI field emission scanning electron microscopy (FE-SEM). The contact angle was measured by the Sessile drop method by placing 5 μL drops on the samples. The images were captured using a digital single-lens reflex (DSLR) camera, and the contact angle was measured with the help of ImageJ software.

After self-aligning the interface pair, the mechanical oscillation for the T-TENGs was supplied by an oscillating force (8 N with 4 Hz frequency) via an electrodynamic shaker system (TIRA, TV 50018, Germany). The oscillating force corresponds to a nominal contact pressure of 12.8 kPa. A peak-to-peak amplitude of 2 mm was configured as the mechanical oscillated separation distance. The output voltage was recorded by an oscilloscope (MSO-X 4154A, KEYSIGHT, USA). The current was measured using the Stanford SR570 low noise current preamplifier connected to the oscilloscope.[23,43] The transferred charge was recorded on a Keithley 6517B electrometer. The surface potential was measured using the Trek 347 noncontact electrostatic voltmeter. The test parameters (contact pressure, frequency, separation distance, etc.) were maintained constant to compare the TENG devices, including different tribolayers and load matching.

Molecular Dynamics Simulation. Flat surfaces of PTFE [Figure S6a] and Fabsil ($C_{32}H_{60}$) [Figure S6d] with dimensions around 19.03 nm × 19.03 nm × 3 nm were formed using the confined layer method[44,45] and have been described in the Supporting Information. PACKMOL was used to make a water droplet (5 nm diameter) with 2170 water molecules such that the density of water remains 0.998 g/cm^3 at 300 K.[46] To observe the wetting behavior of PTFE and Fabsil ($C_{32}H_{60}$) surfaces, respectively, the water droplet was initially placed at a height of 0.2 nm from both the surfaces [Figures S6b,h and S6e]. Then, simulations in the *NVT* ensemble were performed for 500 ps with a time step of 1 fs. The hydrogen atoms in the water molecules were constrained using the SHAKE algorithm. After 300 ps of the abovementioned *NVT* simulations, contact angles were measured every 10 ps until 500 ps using a method reported earlier,[44,47] and then they were time-averaged. OPLSAA force field parameters[48] were used for simulating PTFE and $C_{32}H_{60}$ molecules, while SPCE[49] parameters were used for water molecules and Lorentz−Berthelot rules were

https://doi.org/10.1021/acssuschemeng.3c03620
ACS Sustainable Chem. Eng. 2024, 12, 695−705

applied for getting the Lennard-Jones (LJ) parameters (given in Table S1) between unlike atomic species. Similarly, OPLSAA force field parameters used for simulating interaction between PTFE surfaces and water have been used and validated previously.[44,50] Bonded interaction parameters can be found in previous works. All simulations were run using the LAMMPS[51] software package.

RESULTS AND DISCUSSION

Figure 1a schematically illustrates the concept of artificial leaves-based distributed energy harvesting. The leaf design was carefully structured and implemented to have synergistic operation of TENG and DEG for multisource energy harvesting. The T-TENG device is fabricated using a plasma-treated PTFE (as an electronegative tribolayer) and surface morphology-optimized nylon nanofibril mat (coated on a conductive fabric layer) as the tribo-positive layer. An argon (Ar) plasma treatment was applied onto the T-PTFE textile for device performance optimizations. The T-PTFE was treated with plasma generated at different powers (50, 80, 100, and 150 W) and for different times (3, 6, 9, and 12 min) to find the optimum treatment conditions for the highest power output. Figure 1b,c shows the surface morphology of the pristine and optimized Ar plasma-treated T-PTFE samples. Note that the T-PTFE sample in Figure 1c was treated with Ar plasma at 100 W and 3 min exposure time. The T-PTFE surface got etched to form a ridge pattern (via Ar plasma), which led to a high contact area needed for higher energy conversion efficiency and power output. Generally, the T-PTFE surface is composed of carbon and fluorine atoms, i.e., $-(CF_2-CF_2)_n-$ structured polymer. The presence of unsatisfied (dangling) bonds after plasma treatment has been shown to enhance the performance of TENGs.[52] These energized atoms can serve as surface charge trapping sites to enhance the surface tribo-charge density. In the present case, such bonds were created on the T-PTFE surface because of the plasma treatment. The high impact of Ar^+ ions leads to the defluorination in the PTFE, which produces the unsaturated C−C backbone. Due to the residual oxygen presence, the C−C backbone causes the formation of C−O or C═O bonds.[53] The unsaturated C−C backbone can also form a bond with the fluorine ions. Thus, the unsaturated C−C backbone introduces a high amount of bond defects in the polymer chains of PTFE.[42] The surface roughness of the pristine and plasma-treated T-PTFE textile is shown in Figure S1. Similarly, the morphology of electrospun nylon nanofiber mats was optimized by using the 17, 19, 20, and 22 G needles. Figure 1d shows the SEM image of the fibers obtained by using the 20 G needles. Figure S2 depicts the SEM images of nylon nanofibers prepared by using other needles. The SEM images suggest that the fibers fabricated using 20 G needles are closely packed with low fiber intergaps. The influence of plasma treatment and different nylon nanofibers was analyzed by measuring the output performance of T-TENGs. Figure 2a,b plots the output voltage and short circuit current of the devices for a range of varying processing power (plasma time was fixed to 3 min). The 20G nylon nanofibers were used as the positive triboelectric layer for these experiments. This experimental nylon mat has been calculated to have a crystallinity of 27.8% by using its X-ray diffraction (XRD) patterns in Figure S3. The peak positive voltages and currents are then taken from Figure 2a,b, and output voltage and short circuit current profiles are plotted at different plasma generation powers. The results revealed that the output voltage increased 9.3 times after the plasma treatment was performed at 100 W compared with the pristine film. When the applied power increased further to 150 W, the output voltage decreased from 252 to 85 V. Additionally, the peak positive short circuit current follows the same trend and increases from 6.7 μA for pristine case to 57.6 μA for 100 W, thus presenting an increase of 8.6 times. The short circuit current also declined to 19.3 μA, after the Ar plasma generation power was increased to 150 W. Next, the plasma generation power was fixed at 100W to explore the optimum Ar plasma treatment time for T-PTFE, and the corresponding electrical performance is shown in Figure 2c,d. The peak positive voltages and currents confirm that the output voltage considerably improves from the pristine case (27 V) to the one with 3 min plasma treatment (252 V). However, the output voltage decreases from 252 to 97 V, when the plasma exposure time increases from 3 to 12 min. The experimental observation suggests that the optimum plasma generation power and exposure time for the T-PTFE surface is 100 W and 3 min. A similar trend is also seen in Figure 2e for the transferred charges tested by an electrometer. The maximum transferred charges for the Ar plasma-treated device (i.e., 100 W/3 min) is 246 nC. The same conclusion can be drawn by measuring the transferred charges of the devices, as shown in Figure 2f. In fact, despite the low applied force, the output performances (i.e., 252 V and 9.2 $\mu A/cm^2$) from Ar plasma-treated T-PTFE-based T-TENG are among the highest reported (see the comparison in Table S3).

To further probe the influence of plasma treatment, the surface potential developed by bringing the pristine and Ar plasma-treated sample into multiple contacts with nylon was measured (Figure 2g). Simultaneously, the surface potentials of the nylon layer surfaces, which were in contact with the pristine and Ar plasma-treated T-PTFE, respectively, were also tested, as shown in Figure 2h. The results agree with the obtained electrical performance shown in Figure 2. Thus, the increase in output power can be attributed to the change in the material's properties like surface potential, surface composition, and surface roughness. Furthermore, the effect of different nylon nanofibers on the electrical performance was analyzed and is shown in Figure S4. The 20 G nylon nanofibrous mats produced the best output due to the compact arrangement of the fibers. It is well-known that the output performance of TENGs varies with the external load resistance. Therefore, the output power density is plotted against a range of resistance in Figure 2i, corresponding to the pristine PTFE device (black line) and Ar plasma-treated device (red line). The pristine device exhibits a maximum power density (i.e., 0.23 W/m^2) in the resistance range of 10−20 MΩ, whereas the plasma-treated device shows a maximum power density of 11.4 W/m^2 in the resistance range of 50−100 MΩ. The Ar plasma-treated device shows an increase in the power density by a factor of 49.5 as compared with the pristine device. The energy conversion efficiency of this TENG device is 70.2%, and the device crest factor is 3.6.[54,55] The applicability of the optimum Ar plasma-treated T-PTFE-based device was validated by charging numerous capacitors (with capacitances of 2, 10, and 22 μF) for 200s via a rectifier circuit shown in Figure S5. The capacitor exhibited an obvious trend of increasing charging time (fixed voltage) with the increase in capacitance. The working principle of the T-TENG also has been included in Figure 1a.

Figure 1a also shows the scheme for integration of a T-DEG device on the top of T-TENG. The T-DEG was developed by a T-PTFE layer with different surface treatments for harvesting

https://doi.org/10.1021/acssuschemeng.3c03620
ACS Sustainable Chem. Eng. 2024, 12, 695−705

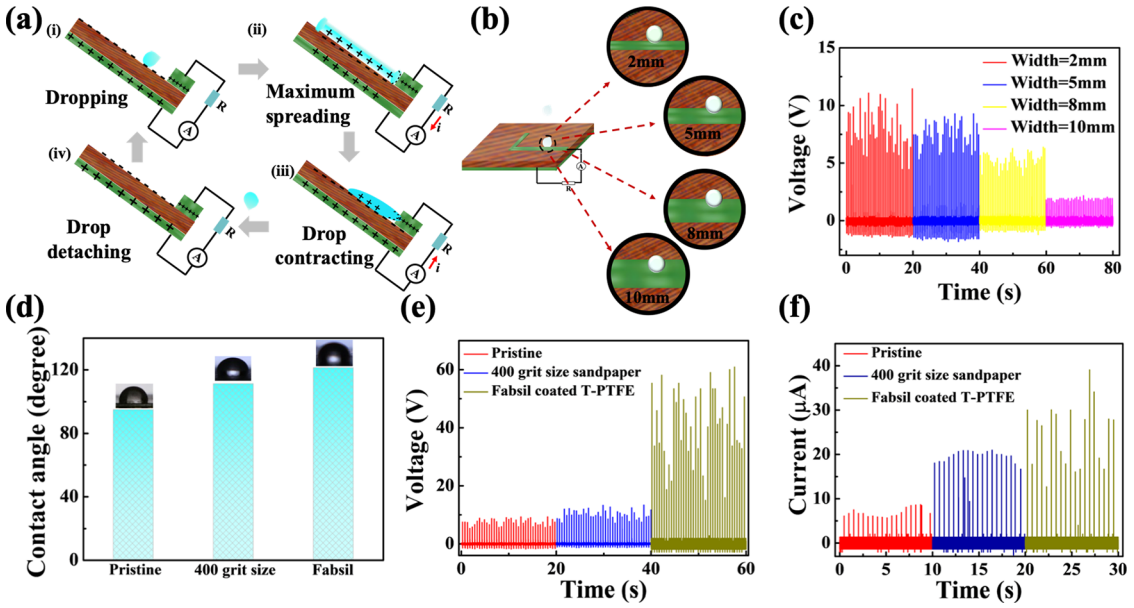

Figure 3. (a) Working of a T-DEG. (b) Schematic illustration of a droplet on the T-DEG devices with different sizes of the top electrode. (c) Voltage generated by DEG with different top electrode widths. (d) Contact angle for the three variations of T-PTFE surface. (e) Output voltage and (f) short circuit current of the T-DEG devices with pristine, sandpaper processed, and waterproofing solution coated T-PTFE.

water droplet energy. In comparison with the single electrode TENGs used for water drop harvesting, DEG uses an additional electrode layer on the device's top surface, which encounters water droplets periodically. The factors affecting the output performance of DEG include the hydrophobicity of the impacted material surface, device bulk effect, drop height, and flow rate.[53] The working principle of the PTFE-based T-DEG is shown schematically in Figure 3a. The continuous impact of water droplets on the material surface results in an accumulation of negative charges on the surface of T-PTFE. The generation of tribo-negative charges on the T-PTFE surface results in the induction of positive charges onto the top and bottom electrodes. Owing to the charge neutrality, the density of the positive charges on the top electrode should be equal to the charge density on the bottom electrode in Figure 3a(i). However, after the droplet encounters the top electrode (i.e., during its spreading), its area gets bigger with droplet spreading, which reduces the charge density of the top electrode, as shown in Figure 3a(ii). Due to the decrease in the charge density of the top electrode, the charge balance in Figure 3a(i) is disturbed, and this drives the bottom electrode charges to the top electrode until the charge density in T-DEG is balanced again, as shown in Figure 3a(ii). The charge transfer between the two electrodes leads to the generation of current output. Figure 3a(iii) elucidates how the contracting droplet starts to reduce the area of the top electrode due to the hydrophobicity of T-PTFE. Because the charge density on the top electrode is higher than the bottom electrode, the charges were transferred in the opposite direction as shown in Figure 3a(iii). There is a closed-circuit loop, which is relatively constructed between the electrodes by the influence of the impacted droplet (i.e., bulk effect 42) during the T-DEG device power generation. Figure 3a(iv) illustrates that the T-DEG stops to generate power when the droplet detaches from the top electrode (i.e., due to the hydrophobicity of the T-PTFE surface). Thus, the present work optimizes the T-DEG performance by tuning the dimension of the top electrode, surface hydrophobicity, and droplet characteristics (flow rate and flow height).

The output of the DEG is influenced by the variation of the spreading droplet area due to the spread of the droplet causing the change of surface charge density on the top electrode.[56] Because of this, electrons were driven to migrate between the two electrodes. Additionally, the DEG literature shows that the output current is largely affected by the area variation ratio of the spreading droplet (i.e., dS/dt), where S is the total area of the device.[56] Additionally, the charge transfer between the top and bottom electrodes only occurs after droplet contact with the top electrode. Namely, the spreading droplet is a part of the top electrode. Thus, the area of the top electrode has an influence on the output performance of the DEG. Figure 3b illustrates the DEG with different top electrode widths of 2, 5, 8, and 10 mm, respectively (length is fixed to 4.5 cm). The copper (Cu) foil was used as the electrodes in these four devices. Figure 3c compares the output voltages of the four abovementioned devices under a 500 mL/h flow rate and 3 cm drop height. The peak positive output voltage decreases as the top electrode width increases. The top electrode with a 2 mm width showed the best output of 11.25 V, followed by 5 mm (9.75 V), 8 mm (6.25 V), and 10 mm (2.3 V) widths. The output voltage increased five times when the top electrode width was reduced from 8 mm to 2 mm. If the droplets were impacted at the same location of these four T-PTFE surfaces, the overlap area between the top electrode and the droplet should increase with the increased area of the top electrode (Figure 3b). The highest change in the dS/dt for the 2 mm top electrode device leads to the generation of the highest output among these four devices. The low overlap area boosts a higher change of the top electrode area (i.e., dS). Note that dt (i.e., contact time between the impact of the droplet and the T-PTFE surface) should be approximately the same in these four situations due to the similar surface hydrophobicity.

The spread and contraction of the water droplet depend on the surface hydrophobicity of the contact material. Thus, tuning the surface hydrophobicity is one of the straightforward

https://doi.org/10.1021/acssuschemeng.3c03620
ACS Sustainable Chem. Eng. 2024, 12, 695−705

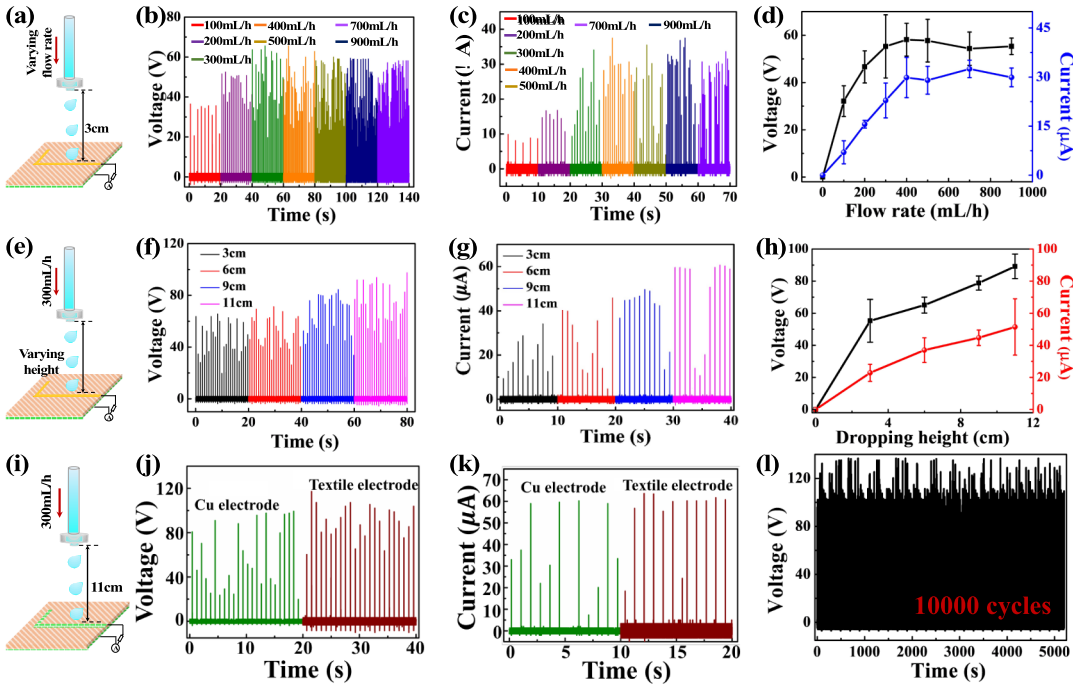

Figure 4. (a) Experiment scheme showing the supplying droplets with varying flow rate and a fixed 3 cm dropping height. (b) output voltage and (c) short circuit current of the T-DEG at different flow rate (copper top electrode). (d) Maximum value of voltage and current versus flow rates. (e) Experiment scheme showing the supplying droplets with a varying height and a fixed 300 mL/h flow rate (f) Output voltage and (g) short circuit current of the T-DEG by different dropping height (copper top electrode). (h) Variation in the voltage and current versus dropping height. (i) Experiment scheme involving the textile top electrode device and supplying droplets at a 11 cm dropping height and a 300 mL/h flow rate. (j) Voltage and (k) current generated by the T-DEGs with copper and conductive textile top electrode. (l) Stability of the fully textile-based T-DEG.

routes to improve DEG performance. To tune the hydrophobicity, inspired by the water-repellent behavior of the lotus leaves ("lotus effect"), we have performed biomimicry of the lotus effect to achieve a highly hydrophobic textile surface and thus enhance the output power. The surface hydrophobicity can be improved by roughening the surface, using low surface energy materials, creating air pockets on the material surface, constructing micro- or nanoscale structures, or coating the surface with chemicals [e.g., tetrafluoroethylene (TFE) and wax]. The T-PTFE film was processed by the sandpapers (i.e., 400 grit sizes) and a commercial waterproofing solution (Fabsil-60% naphtha) to analyze the enhancement of DEG output performance with improved surface hydrophobicity. The change in the contact angle due to the Fabsil coating was studied by the MD simulations, as shown in Figure S6. Figure 3d experimentally compares the surface hydrophobicity for each of the three T-PTFE films by the contact angle measurement. The surface hydrophobicity of the sandpaper and waterproof coated T-PTFE films is higher than the pristine T-PTFE. The contact angle of the films was increased from 95° (pristine) to 115.6° (400 grit sizes) and 121.3° (Fabsil). Figure 3e,f depicts the measured outputs (i.e., output voltage and short circuit current) of the DEG devices with T-PTFE films having different surface hydrophobicity. These measurements were performed at a flow rate and dropping height of 500 mL/h and 3 cm, respectively, and under a 1MΩ load resistance. The peak positive output voltage was 11.25 (pristine), 13.75 (400 grit sizes), and 59.6 V (Fabsil), i.e., 5.3 times increase from pristine to waterproofing coating. Like TENGs, DEGs are also high voltage and low current devices; therefore, the critical requirement is to boost the current density of the DEG. As shown in Figure 3f, the peak short circuit current was about 7.3 μA for the pristine case, 20 μA for the 400 grit size processed T-PTFE device, and a maximum of 30 μA for the waterproofing coated T-PTFE device, representing an increase of 4.1 times over the pristine case. The contact time of a droplet decreases as the surface hydrophobicity increases.[57] The high dS/dt corresponds to high output, and it can be obtained on surfaces with high hydrophobicity as it takes a lower time for a drop to spread and contract on hydrophobic surfaces. Furthermore, Figure S7 illustrates the output power and current of the optimal T-DEG device in relation to the resistive load. These measurements were conducted at a flow rate of 500 mL/h and a drop height of 3 cm.

Figure 4 shows the T-DEG test setup for device characterization and the output performance of DEG with different droplet flow rates and dropping height. Figure 4a–d shows the measuring setup, output voltage, and current signals for seven flow rates varying between 100 to 900 mL/h under a fixed 3 cm dropping height. The peak positive output voltages and short circuit current are extracted from Figure 4b,c and plotted against the flow rate in Figure 4d. The output voltage increases with a flow rate up to 300 mL/h, and beyond 300 mL/h, the output voltage saturates at a value of around 58 V. A similar trend was also obtained for the short circuit current. Short circuit current grows with the flow rate, and the upper end of the flow rate range is also adequate to saturate the short circuit current; that is, beyond 400 mL/h, the short circuit current levels off at around 30 μA. After evaluation of the droplet flow rate, the effect of the dropping heights was investigated. Figure 4e–h shows the measurement setup and performances of a T-DEG for the 3 to 11 cm dropping height with the flow rate fixed to 300 mL/h. Figure 4h plots the T-DEG outputs against the dropping heights. The positive peak output voltage rises

https://doi.org/10.1021/acssuschemeng.3c03620
ACS Sustainable Chem. Eng. 2024, 12, 695−705

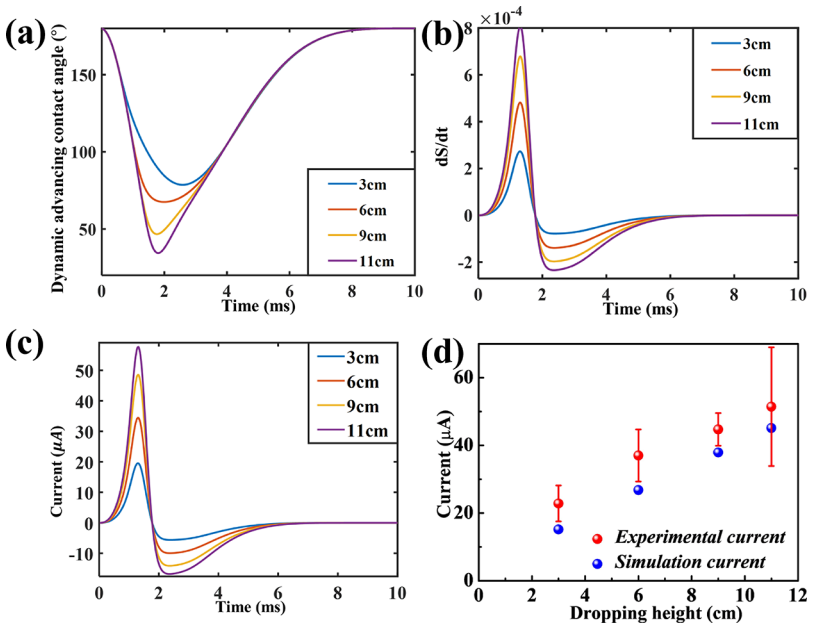

Figure 5. T-DEG simulation results. (a) Simulated dynamic contact angle of a droplet impacting onto the T-PTFE surface. (b) Simulated results of dS/dt. (c) Simulated short circuit current at different dropping height. (d) Comparisons of the experimental and simulated results of the short circuit current at different dropping height.

from 58 to 90 V, corresponding to an increase in the dropping height from 3 to 11 cm. Comparably, the short circuit current of the T-DEG increases approximately linearly (from 20 to 52 μA) with the increasing dropping height until 11 cm, as shown in Figure 4h. The top copper electrode of T-DEG was replaced with a conductive fabric electrode (Ni/Cu polyester fabric tape with conducting adhesive) to obtain a fully textile-based DEG, as shown in Figure 4i. The outputs from the conductive fabric electrode device are comparable with those of the Cu electrode-based device. The output of the conductive fabric electrode-based device was measured under a 300 mL/h flow rate and 11 cm dropping height. The output voltage (113 V) and short circuit current (67 μA) of the conductive fabric electrode device were slightly higher than the 95 V and 58 μA outputs of Cu electrode-based T-DEG (Figure 4j, k). The slight increase in the output can be ascribed to the better sliding of the droplets on the textile electrode. The comparison of T-DEG with previous works on textile-based water drop energy generators is given in Table S2. Comparing the water droplet-based electricity generation by T-TENGs (single electrode and freestanding modes, i.e., SE-TENG and F-TENG), the T-DEG exhibits higher performance, as may be noted from Table S2. The present work shows significantly higher outputs compared with the other reported textile-based DEGs. The high output current in this work could be largely attributed to the effect of the high tribo-negative property of the polymer and the waterproof coating. The developed conductive fabric electrode T-DEG also showed high stability toward the applied periodic droplet cycles. The output voltage of T-DEG, based on conductive fabric electrodes and waterproofing coated T-PTFE textile, was measured for up to 10,000 cycles at 1 MΩ load resistance under 400 mL/h flow rate and 11 cm dropping height, as shown in Figure 4l. The stable output voltage (around 113 V) for up to 10000 cycles confirms excellent device stability.

Understanding the dynamics of a droplet's impact on a solid surface can help to enhance the DEG output power. There are a number of important implications that follow from the view that DEG electrical performance is dependent on a periodic morphological change for the impacted droplet. The working principle of a DEG power generation depends on the area change ratio of the top electrode (i.e., dS/dt) due to droplet spreading (see eqs S1 and S2). Thus, if we import the characterization of droplet spreading on a hydrophobic surface, it can be used to fully explain the factors for the change of the top electrode area. The variable ratio of a droplet can be described by $\beta_{max}=\frac{d_{max}}{d_0}$.[57] The β_{max} is the ratio between the maximum spreading diameter and the initial drop diameter. However, β_{max} is influenced by the droplet properties and impact velocity, which characterize the inertial and surface tension effects. The vertical kinetic energy of a droplet is transferred to the radial direction to boost the droplet spreading after the droplet hits against the surface.[57] After a droplet contacts the hydrophobic surface, there are four scenarios, i.e., spread, maximum spread, contract, and detaching away from the surface. The droplet experiences deformation due to the transformation of kinetic energy from the dropping height and velocity. Employing the Weber number and dynamic contact angle, we can evaluate the normal impact on a hydrophobic surface as[57]:

$$\beta_{max} = 1 + \frac{8}{27}\sqrt{\frac{We}{3\sigma(1-\cos\theta_{\alpha,max})}} \quad (1)$$

$$We = \frac{\rho {\mu_0}^2 d_0}{\sigma} \quad (2)$$

where θ_α is the dynamic advancing contact angle. We is the dimensionless number (i.e., Weber number). ρ, μ_0, d_0, and σ are liquid density, impact velocity, initial droplet diameter, and liquid surface tension. First, the characterization of d_{max} for a droplet impacting on a solid hydrophobic surface can be calculated by

https://doi.org/10.1021/acssuschemeng.3c03620
ACS Sustainable Chem. Eng. 2024, 12, 695−705

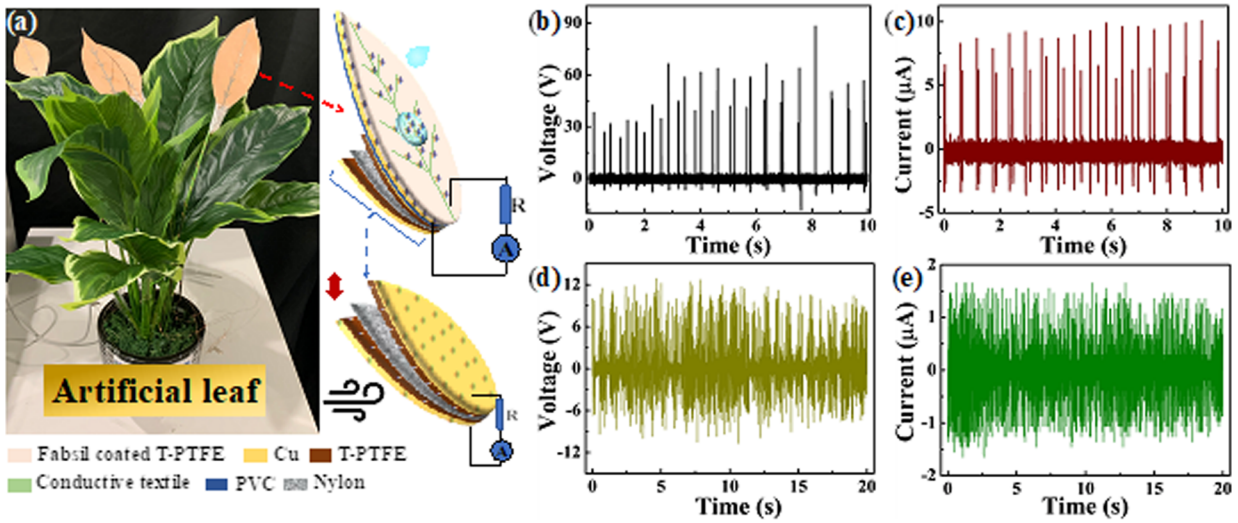

Figure 6. (a) Schematic image of artificial leaf-shaped multisource energy generator. Output performance of harvesting droplets dropping energy, (b) output voltage, and (c) short circuit current. Output performance of harvesting wind power, (d) output voltage, and (e) short circuit current.

$$d_{max} = d_0 + \frac{8d_0}{27}\sqrt{\frac{\rho {\mu_0}^2 d_0}{3\sigma(1-\cos\theta_{\alpha,min})}} \quad (3)$$

if consider the spread droplet is a cycle,

$$S(t) = \pi\left(\frac{d_0}{2} + \frac{4d_0\mu_0}{27}\sqrt{\frac{\rho d_0}{3\sigma(1-\cos\theta_\alpha(t))}}\right)^2 \quad (4)$$

Integrating eqs 3 and 4 into DEG output current formula eq 5,[56]

$$I_{out} = \frac{-\sigma_T}{2}\frac{dS(t)}{dt} \quad (5)$$

Figure 5a estimates the variation of the dynamic contact angle during one cycle (i.e., from dropping to detaching) of the droplet impacting the T-PTFE surface under 3 cm dropping height. The dynamic contact angle between the droplet and substrate decreases continuously in the compression phase, while the dynamic contact angle starts to increase again during the restoring status. Figure 5b,c presents the device's simulated dS/dt and output current signal with a dropping height from 3 to 11 cm using numerical analysis methods (i.e., MATLAB simulation). Note that the surface charge density (i.e., σ_T) is equal to $-113.06\ \mu C/m^2$.[58] From experimental results and eq S2, one of the key parameters for droplet spreading and DEG outputs is the impact velocity (μ_0). Additionally, the impact velocity increases with increasing dropping height from 3 to 11 cm. After considering the effect of the air friction on the droplets, the impact velocity can be calculated via $\mu_0 = \sqrt{\frac{g}{\alpha}(1-\exp(-2\alpha h))}$. Simultaneously, $\alpha = \frac{3C_f\rho_{air}}{8\rho_{water}R_0}$, where g, h, ρ_{air}, ρ_{water}, R_0, and C_f are the gravitational constant = 9.8 m/s^2, dropping height, density of air and water, droplet radius, and adjusted friction coefficient = 0.796.[59] The results in Figure 4h also support the fact that the output of T-DEG is highly dependent on the drop falling height. The comparison of experimental and simulated current outputs in Figure 5d follows the dS/dt results shown in Figure 5b. When droplet height increases from 3 to 11 cm, the short circuit current increases by a factor of 2.6 in the experimental results, while simulations predict an almost similar increase in short circuit current (roughly 2.8 times). Thus, it can be said that the T-DEG output current is dependent on the dropping height via the impact velocity. Additionally, the high droplet flow rate enhances the transfer of the charges between the top and bottom electrode (i.e., ΔQ). The outputs improve after the flow rate increases from 100 to 300 mL/h. However, when the droplet flow rate is over 400 mL/h, a water layer remains on the T-PTFE surface due to a higher number of drops in a given time, leading to the constant output after 400 mL/h.

Following the optimization studies, the leaf-shaped design was implemented for integrated T-TENG and T-DEG to harvest the energy from multiple ambient sources and realize a self-powered system. Figure 6 shows the developed synthetic leaf, which is driven by wind and waterdrops to power the LEDs. Figure 6a illustrates the structure of this leaf-shaped device as having a top T-DEG layer (for droplet energy harvesting) and a bottom contact-separation mode free-standing TENG (CSF-TENG) layer (for wind power harvesting). Note that the width of the electrode with a vein-like structure for our T-DEG is fixed at 2 mm. The CSF-TENG tribo-contact layers were a nylon fibrous mat and Ar plasma-treated T-PTFE layers. The fabrication procedures of this leaf-shaped multisource energy harvester are shown in Figure S8. Four synthetic leaves were implanted into a commercial artificial plant, and the device outputs were measured under the random perturbations from rain drops and wind. With droplets impacting the DEG, the maximum output voltage and short circuit current could reach up to 67.5 V and 10 μA, respectively, as shown in Figure 6b,c. Simultaneously, the highest output voltage and short circuit current for wind energy harvesting can be 12 V and 1.75 μA, respectively, as shown in Figure 6d,e. Comparing the output results in Figures 2 and 4 with the artificial leaf-shape device in Figure 6, we observed that the output of the artificial leaf-shape device is lower. This could be attributed to the fact that measurement results shown in Figure 6 are obtained under conditions mimicking natural conditions, i.e., moderate rainfall and low wind. For example, random droplets may not be hitting the top electrode at the optimum location, which is essential for achieving the best device performance considering the mechanism of DEG explained earlier [Figure 3b, c]. Addition-

https://doi.org/10.1021/acssuschemeng.3c03620
ACS Sustainable Chem. Eng. 2024, 12, 695−705

ally, when the device was used for harvesting wind energy, there was a low contact pressure between the interface pair, which resulted in a low real contact area and output performance.[41] To demonstrate the degree of energy generated by artificial leaves, the output was used to power 10 LEDs via a rectifier circuit (see Figure S9). The LED array was turned on using the power harnessed via droplets or wind energy, as shown in Video S1. Considering these results, the leaf-shaped energy generator can be an effective source to light up places such as coastal areas and mountains, where sufficient electricity sources are not available. These results also exhibit enormous potential for practical applications in green energy harvesting to power distributed IoT devices and smart lighting in homes and public spaces.

CONCLUSIONS

Here, for the first time, we presented a textile-based TENG synergistic integrated with DEG using selected materials and innovative design. For T-TENG, the performance was enhanced by Ar plasma treatment on the PTFE layer and by optimizing the surface morphology of the positive nylon triboelectric layer. An Ar plasma treatment at 100W for 3 min improved the output performance of the T-TENG device to 252 V and 57.6 μA, which represents 9.3 and 8.6 times increase in voltage and current, respectively, compared with the pristine device. On the other hand, the DEG performance depends on the hydrophobicity of the droplet impact surface. The hydrophobic T-PTFE textile surface was prepared by coating the waterproofing solution (i.e., Fabsil) approach, which can generate significantly higher outputs (113 V and 67 μA) at a lower flow rate of 300 mL/h and 11 cm dropping height. The T-DEGs were systematically studied to understand and optimize the design of DEGs, including top electrode size, surface hydrophobicity, dropping height, and flow rate. A new DEG model is also proposed to understand the mechanism of power generation. Comparing the experimental and simulated results, this work evaluated the influence of droplet area variation on the DEG output performance. Finally, the textile-based TENG and DEG are assembled as a synthetic leaf to demonstrate multisource energy harvesting. The simple, and low-cost energy-generating leaf prototype effectively harvests the wind and raindrop energy to power 10 LEDs. Such proof-of-concept devices could be further advanced to develop energy-harvesting artificial trees to produce clean energy everywhere from gentle winds and rain drops.

ASSOCIATED CONTENT

Supporting Information

The Supporting Information is available free of charge at https://pubs.acs.org/doi/10.1021/acssuschemeng.3c03620.

Surface roughness, SEM images, output performances for the device with different nylon layers, energy stored in various capacitors, molecular dynamics simulation, textile-based leaf-shaped multisource energy generator, and its equivalent energy harvesting circuit (DOCX)

LED array turned on using the power harnessed via droplets or wind energy (MP4)

Artificial tree information (MOV)

AUTHOR INFORMATION

Corresponding Author

Ravinder Dahiya − *Bendable Electronics and Sustainable Technologies (BEST) Group, Electrical and Computer Engineering Department, Northeastern University, Boston, Massachusetts 02115, United States;* orcid.org/0000-0002-3858-3841; Email: r.dahiya@northeastern.edu

Authors

Guanbo Min − *CAS Center for Excellence in Nanoscience, Beijing Key Laboratory of Micro-nano Energy and Sensor, Beijing Institute of Nanoenergy and Nanosystems, Chinese Academy of Sciences, Beijing 101400, China; School of Nanoscience and Technology, University of Chinese Academy of Sciences, Beijing 100049, China*

Gaurav Khandelwal − *James Watt School of Engineering, University of Glasgow, Glasgow G12 8QQ, U.K.;* orcid.org/0000-0002-7698-4494

Abhishek Singh Dahiya − *James Watt School of Engineering, University of Glasgow, Glasgow G12 8QQ, U.K.;* orcid.org/0000-0003-4509-2650

Shashank Mishra − *James Watt School of Engineering, University of Glasgow, Glasgow G12 8QQ, U.K.*

Wei Tang − *CAS Center for Excellence in Nanoscience, Beijing Key Laboratory of Micro-nano Energy and Sensor, Beijing Institute of Nanoenergy and Nanosystems, Chinese Academy of Sciences, Beijing 101400, China; School of Nanoscience and Technology, University of Chinese Academy of Sciences, Beijing 100049, China*

Complete contact information is available at: https://pubs.acs.org/10.1021/acssuschemeng.3c03620

Author Contributions

G.M., G.K., and R.D. designed the experiments; G.M., G.K., and A.S.D. prepared and conducted the experiments; G.M., G.K., A.S.D., and S.M. analyzed the experimental data. S.M. conducted the numerical simulation and Molecular dynamics simulation; R.D. provided overall supervision of the project, and all authors contributed to the general discussion. All authors have given approval to the final version of the manuscript.

Notes

The authors declare no competing financial interest.

ACKNOWLEDGMENTS

This work was started by R. Dahiya's Bendable Electronics and Sensing Technologies (BEST) Group. G.M. was also a member of this group at that time. The work was completed after R. Dahiya moved to Northeastern University, where his group is known as Bendable Electronics and Sustainable Technologies (BEST) Group.

REFERENCES

(1) Rehmani, M. H.; Pathan, A.-S. K. Emerging Communication Technologies Based on Wireless Sensor Networks: *Current Research and Future Applications*, **2016**.

(2) Nagajayanthi, B. Decades of Internet of Things Towards Twenty-First Century: A Research-Based Introspective. *Wirel. Pers. Commun.* **2022**, *123* (4), 3661−3697.

(3) Friha, O.; Ferrag, M. A.; Shu, L.; Maglaras, L.; Wang, X. Internet of Things for the Future of Smart Agriculture: A Comprehensive Survey of Emerging Technologies. *IEEE-CAA J. Automatica Sin.* **2021**, *8* (4), 718−752.

(4) Murali, P. K.; Kaboli, M.; Dahiya, R. Intelligent In-Vehicle Interaction Technologies. *Adv. Intell. Syst.* **2022**, *4* (2), No. 2100122.
(5) Manjakkal, L.; Mitra, S.; Petillot, Y. R.; Shutler, J.; Scott, E. M.; Willander, M.; Dahiya, R. Connected Sensors, Innovative Sensor Deployment, and Intelligent Data Analysis for Online Water Quality Monitoring. *IEEE Internet Things J.* **2021**, *8* (18), 13805−13824.
(6) Manjakkal, L.; Yin, L.; Nathan, A.; Wang, J.; Dahiya, R. Energy Autonomous Sweat-Based Wearable Systems. *Adv. Mater.* **2021**, *33* (35), No. 2100899.
(7) Zhou, Z.; Chen, N.; Zhong, H.; Zhang, W.; Zhang, Y.; Yin, X.; He, B. Textile-Based Mechanical Sensors: A Review. *Materials* **2021**, *14* (20), 6073.
(8) Blachowicz, T.; Ehrmann, G.; Ehrmann, A. Textile-Based Sensors for Biosignal Detection and Monitoring. *Sensors* **2021**, *21* (18), 6042.
(9) Coyle, S.; Morris, D.; Lau, K.-T.; Diamond, D.; Moyna, N. Textile-Based Wearable Sensors for Assisting Sports Performance. In *2009 Sixth International Workshop on Wearable and Implantable Body Sensor Networks*, 2009; pp 307−311.
(10) Escobedo, P.; Bhattacharjee, M.; Nikbakhtnasrabadi, F.; Dahiya, R. Flexible Strain and Temperature Sensing NFC Tag for Smart Food Packaging Applications. *IEEE Sens. J.* **2021**, *21* (23), 26406−26414.
(11) Tabor, J.; Chatterjee, K.; Ghosh, T. K. Smart Textile-Based Personal Thermal Comfort Systems: Current Status and Potential Solutions. *ADV MATER TECHNOL-US* **2020**, *5* (5), No. 1901155.
(12) O'Neill, C. T.; McCann, C. M.; Hohimer, C. J.; Bertoldi, K.; Walsh, C. J. Unfolding Textile-Based Pneumatic Actuators for Wearable Applications. *Soft Robot.* **2022**, *9* (1), 163−172.
(13) Meng, K.; Zhao, S.; Zhou, Y.; Wu, Y.; Zhang, S.; He, Q.; Wang, X.; Zhou, Z.; Fan, W.; Tan, X.; Yang, J.; Chen, J. A Wireless Textile-Based Sensor System for Self-Powered Personalized Health Care. *Matter* **2020**, *2* (4), 896−907.
(14) Chen, X.; He, H.; Khan, Z.; Sydänheimo, L.; Ukkonen, L.; Virkki, J. Textile-Based Batteryless Moisture Sensor. *IEEE Antennas Wirel. Propag. Lett.* **2020**, *19* (1), 198−202.
(15) Nikbakhtnasrabadi, F.; El Matbouly, H.; Ntagios, M.; Dahiya, R. Textile-Based Stretchable Microstrip Antenna with Intrinsic Strain Sensing. *ACS Appl. Electron. Mater.* **2021**, *3* (5), 2233−2246.
(16) Neto, J.; Chirila, R.; Dahiya, A. S.; Christou, A.; Shakthivel, D.; Dahiya, R. Skin-Inspired Thermoreceptors-Based Electronic Skin for Biomimicking Thermal Pain Reflexes. *Adv. Sci.* **2022**, *9* (27), No. 2201525.
(17) Liu, F.; Deswal, S.; Christou, A.; Sandamirskaya, Y.; Kaboli, M.; Dahiya, R. Neuro-Inspired Electronic Skin for Robots. *Sci. Robot.* **2022**, *7* (67), No. eabl7344.
(18) Khandelwal, G.; Dahiya, R. Self-Powered Active Sensing Based on Triboelectric Generators. *Adv. Mater.* **2022**, *34* (33), No. 2200724.
(19) Kang, D. H. P.; Chen, M.; Ogunseitan, O. A. Potential Environmental and Human Health Impacts of Rechargeable Lithium Batteries in Electronic Waste. *Environ. Sci. Technol.* **2013**, *47* (10), 5495−5503.
(20) Melchor-Martínez, E. M.; Macias-Garbett, R.; Malacara-Becerra, A.; Iqbal, H. M. N.; Sosa-Hernández, J. E.; Parra-Saldívar, R. Environmental Impact of Emerging Contaminants from Battery Waste: A Mini Review. *Case Stud. Therm. Eng.* **2021**, *3*, No. 100104.
(21) Hosseini, E. S.; Dervin, S.; Ganguly, P.; Dahiya, R. Biodegradable Materials for Sustainable Health Monitoring Devices. *ACS Appl. Bio. Mater.* **2021**, *4* (1), 163−194.
(22) Chakraborty, M.; Kettle, J.; Dahiya, R. Electronic Waste Reduction Through Devices and Printed Circuit Boards Designed for Circularity. *J-FLEX* **2022**, *1* (1), 4−23.
(23) Min, G.; Pullanchiyodan, A.; Dahiya, A. S.; Hosseini, E. S.; Xu, Y.; Mulvihill, D. M.; Dahiya, R. Ferroelectric-Assisted High-Performance Triboelectric Nanogenerators Based on Electrospun P(VDF-TrFE) Composite Nanofibers with Barium Titanate Nanofillers. *Nano Energy* **2021**, *90*, No. 106600.
(24) Jiang, D.; Liu, G.; Li, W.; Bu, T.; Wang, Y.; Zhang, Z.; Pang, Y.; Xu, S.; Yang, H.; Zhang, C. A Leaf-Shaped Triboelectric Nanogenerator for Multiple Ambient Mechanical Energy Harvesting. *IEEE Trans. Power Electron.* **2020**, *35* (1), 25−32.
(25) Feng, Y.; Zhang, L.; Zheng, Y.; Wang, D.; Zhou, F.; Liu, W. Leaves Based Triboelectric Nanogenerator (TENG) and TENG Tree for Wind Energy Harvesting. *Nano Energy* **2019**, *55*, 260−268.
(26) Chu, S.; Majumdar, A. Opportunities and Challenges for a Sustainable Energy Future. *Nature* **2012**, *488* (7411), 294−303.
(27) Escobedo, P.; Ntagios, M.; Shakthivel, D.; Navaraj, W. T.; Dahiya, R. Energy Generating Electronic Skin With Intrinsic Tactile Sensing Without Touch Sensors. *IEEE Trans. Robot* **2021**, *37* (2), 683−690.
(28) Meder, F.; Thielen, M.; Mondini, A.; Speck, T.; Mazzolai, B. Living Plant-Hybrid Generators for Multidirectional Wind Energy Conversion. *Energy Technol.* **2020**, *8* (7), No. 2000236.
(29) Xu, X.; Wang, Y.; Li, P.; Xu, W.; Wei, L.; Wang, Z.; Yang, Z. A Leaf-Mimic Rain Energy Harvester by Liquid-Solid Contact Electrification and Piezoelectricity. *Nano Energy* **2021**, *90*, No. 106573.
(30) Min, G.; Xu, Y.; Cochran, P.; Gadegaard, N.; Mulvihill, D. M.; Dahiya, R. Origin of the Contact Force-Dependent Response of Triboelectric Nanogenerators. *Nano Energy* **2021**, *83*, No. 105829.
(31) Min, G.; Manjakkal, L.; Mulvihill, D. M.; Dahiya, R. S. Triboelectric Nanogenerator With Enhanced Performance via an Optimized Low Permittivity Substrate. *IEEE Sens. J.* **2020**, *20* (13), 6856−6862.
(32) Dong, K.; Hu, Y.; Yang, J.; Kim, S.-W.; Hu, W.; Wang, Z. L. Smart Textile Triboelectric Nanogenerators: Current Status and Perspectives. *MRS Bull.* **2021**, *46* (6), 512−521.
(33) Wang, S.; Xie, Y.; Niu, S.; Lin, L.; Wang, Z. L. Freestanding Triboelectric-Layer-Based Nanogenerators for Harvesting Energy from a Moving Object or Human Motion in Contact and Non-Contact Modes. *Adv. Mater.* **2014**, *26* (18), 2818−2824.
(34) Gang, X.; Guo, Z. H.; Cong, Z.; Wang, J.; Chang, C.; Pan, C.; Pu, X.; Wang, Z. L. Textile Triboelectric Nanogenerators Simultaneously Harvesting Multiple "High-Entropy" Kinetic Energies. *ACS Appl. Mater. Inter* **2021**, *13* (17), 20145−20152.
(35) Eadie, L.; Ghosh, T. K. Biomimicry in Textiles: Past, Present and Potential An Overview. *J. R Soc. Interface* **2011**, *8* (59), 761−775.
(36) Xiong, J.; Cui, P.; Chen, X.; Wang, J.; Parida, K.; Lin, M.-F.; Lee, P. S. Skin-Touch-Actuated Textile-Based Triboelectric Nanogenerator with Black Phosphorus for Durable Biomechanical Energy Harvesting. *Nat. Commun.* **2018**, *9* (1), 4280.
(37) Zhao, Y.; Fang, F. A Biomimetic Textile with Self-Assembled Hierarchical Porous Fibers for Thermal Insulation. *ACS Appl. Mater. Inter* **2022**, *14* (22), 25851−25860.
(38) Ribul, M.; Lanot, A.; Tommencioni Pisapia, C.; Purnell, P.; McQueen-Mason, S. J.; Baurley, S. Mechanical, Chemical, Biological: Moving towards Closed-Loop Bio-Based Recycling in a Circular Economy of Sustainable Textiles. *J. Clean Prod* **2021**, *326*, No. 129325.
(39) Engelhardt, S.; Sarsour, J. Solar Heat Harvesting and Transparent Insulation in Textile Architecture Inspired by Polar Bear Fur. *Energy Build.* **2015**, *103*, 96−106.
(40) Teodorescu, M. Applied Biomimetics: A New Fresh Look of Textiles. *J. Text.* **2014**, *2014*, 1−9.
(41) Xiong, J.; Lin, M.-F.; Wang, J.; Gaw, S. L.; Parida, K.; Lee, P. S. Wearable All-Fabric-Based Triboelectric Generator for Water Energy Harvesting. *Adv. Energy Mater.* **2017**, *7* (21), No. 1701243.
(42) Xu, W.; Zheng, H.; Liu, Y.; Zhou, X.; Zhang, C.; Song, Y.; Deng, X.; Leung, M.; Yang, Z.; Xu, R. X.; Wang, Z. L.; Zeng, X. C.; Wang, Z. A Droplet-Based Electricity Generator with High Instantaneous Power Density. *Nature* **2020**, *578* (7795), 392−396.
(43) Mallineni, S. S. K.; Behlow, H.; Podila, R.; Rao, A. M. A Low-Cost Approach for Measuring Electrical Load Currents in Triboelectric Nanogenerators. *Nanotechnol. Rev.* **2018**, *7* (2), 149−156.
(44) Zhao, L.; Cheng, J. Analyzing the Molecular Kinetics of Water Spreading on Hydrophobic Surfaces via Molecular Dynamics Simulation. *Sci. Rep.* **2017**, *7* (1), 10880.

https://doi.org/10.1021/acssuschemeng.3c03620
ACS Sustainable Chem. Eng. 2024, 12, 695−705

(45) Hirvi, J. T.; Pakkanen, T. A. Molecular Dynamics Simulations of Water Droplets on Polymer Surfaces. *J. Chem. Phys.* **2006**, *125* (14), 144712.
(46) Martínez, L.; Andrade, R.; Birgin, E. G.; Martínez, J. M. PACKMOL: A Package for Building Initial Configurations for Molecular Dynamics Simulations. *J. Comput. Chem.* **2009**, *30* (13), 2157−2164.
(47) Webb, E. B.; Grest, G. S.; Heine, D. R.; Hoyt, J. J. Dissolutive Wetting of Ag on Cu: A Molecular Dynamics Simulation Study. *Acta Mater.* **2005**, *53* (11), 3163−3177.
(48) Jorgensen, W. L.; Maxwell, D. S.; Tirado-Rives, J. Development and Testing of the OPLS All-Atom Force Field on Conformational Energetics and Properties of Organic Liquids. *J. Am. Chem. Soc.* **1996**, *118* (45), 11225−11236.
(49) Berendsen, H. J. C.; Grigera, J. R.; Straatsma, T. P. The Missing Term in Effective Pair Potentials. *J. Phys. Chem.* **1987**, *91* (24), 6269−6271.
(50) Włoch, J.; Terzyk, A. P.; Wiśniewski, M.; Kowalczyk, P. Nanoscale Water Contact Angle on Polytetrafluoroethylene Surfaces Characterized by Molecular Dynamics−Atomic Force Microscopy Imaging. *Langmuir* **2018**, *34* (15), 4526−4534.
(51) Thompson, A. P.; Aktulga, H. M.; Berger, R.; Bolintineanu, D. S.; Brown, W. M.; Crozier, P. S.; Iint Veld, P. J.; Kohlmeyer, A.; Moore, S. G.; Nguyen, T. D.; Shan, R.; Stevens, M. J.; Tranchida, J.; Trott, C.; Plimpton, S. J. LAMMPS - a Flexible Simulation Tool for Particle-Based Materials Modeling at the Atomic, Meso, and Continuum Scales. *Comput. Phys. Commun.* **2022**, *271*, No. 108171.
(52) Prada, T.; Harnchana, V.; Lakhonchai, A.; Chingsungnoen, A.; Poolcharuansin, P.; Chanlek, N.; Klamchuen, A.; Thongbai, P.; Amornkitbamrung, V. Enhancement of Output Power Density in a Modified Polytetrafluoroethylene Surface Using a Sequential O2/Ar Plasma Etching for Triboelectric Nanogenerator Applications. *Nano Res.* **2022**, *15* (1), 272−279.
(53) Zhang, Q.; Jiang, C.; Li, X.; Dai, S.; Ying, Y.; Ping, J. Highly Efficient Raindrop Energy-Based Triboelectric Nanogenerator for Self-Powered Intelligent Greenhouse. *ACS Nano* **2021**, *15* (7), 12314−12323.
(54) Chen, P.; An, J.; Cheng, R.; Shu, S.; Berbille, A.; Jiang, T.; Wang, Z. L. Rationally Segmented Triboelectric Nanogenerator with a Constant Direct-Current Output and Low Crest Factor. *Energy Environ. Sci.* **2021**, *14* (8), 4523−4532.
(55) Chen, H.; Xu, Y.; Zhang, J.; Wu, W.; Song, G. Theoretical System of Contact-Mode Triboelectric Nanogenerators for High Energy Conversion Efficiency. *Nanoscale Res. Lett.* **2018**, *13* (1), 346.
(56) Wang, X.; Fang, S.; Tan, J.; Hu, T.; Chu, W.; Yin, J.; Zhou, J.; Guo, W. Dynamics for Droplet-Based Electricity Generators. *Nano Energy* **2021**, *80*, No. 105558.
(57) Khojasteh, D.; Kazerooni, M.; Salarian, S.; Kamali, R. Droplet Impact on Superhydrophobic Surfaces: A Review of Recent Developments. *J. Ind. Eng. Chem.* **2016**, *42*, 1−14.
(58) Zou, H.; Zhang, Y.; Guo, L.; Wang, P.; He, X.; Dai, G.; Zheng, H.; Chen, C.; Wang, A. C.; Xu, C.; Wang, Z. L. Quantifying the Triboelectric Series. *Nat. Commun.* **2019**, *10* (1), 1427.
(59) Roux, D. C. D.; Cooper-White, J. J. Dynamics of Water Spreading on a Glass Surface. *J. Colloid Interface Sci.* **2004**, *277* (2), 424−436.

https://doi.org/10.1021/acssuschemeng.3c03620
ACS Sustainable Chem. Eng. 2024, 12, 695−705